obtained within the ESF-QUEEN project; ice sheet thicknesses for the rest of the Northern Hemisphere obtained using the climatic index method[24] applied to an ice sheet model and AGCM outputs[25]; modelled global sea surface temperatures and sea-ice extent[26], surface albedo and roughness over ice-free surfaces derived from modelled glacial maximum palaeovegetation[27]; a large lake in the part of the Baltic Sea depression not covered by the Scandinavian ice sheet[4]; and reconstructed proglacial lakes in European Russia and in West Siberia[3].

Initial conditions and spin-up

The simulations were started from an initial state with present-day soil temperatures. From the 15 yr of each simulation, the first five years were discarded as spin-up. Lake temperatures at the bottom level (between 15 and 30 m) were in equilibrium at the end of the 5 spin-up years. At the end of each of the first three spin-up years for the 90-kyr-ago simulations, soil temperature, being the slowest simulated component of the climate system simulated here, was separately spun up for 1,000 yr using the year's modelled monthly surface temperatures.

Received 15 May; accepted 14 November 2003; doi:10.1038/nature02233.

1. Hostetler, S. W., Bartlein, P. J., Clark, P. U., Small, E. E. & Solomon, A. M. Simulated influences of Lake Agassiz on the climate of central North America 11,000 years ago. *Nature* **405,** 334–337 (2000).
2. Svendsen, J. I. *et al.* Late Quaternary ice sheet history of Eurasia. *Quat. Sci. Rev* (in the press).
3. Mangerud, J., Astakhov, V., Jakobsson, M. & Svendsen, J. I. Huge ice-age lakes in Russia. *J. Quat. Sci.* **16,** 773–777 (2001).
4. Lundquist, J. Glacial stratigraphy in Sweden. *Spec. Pap. Geol. Surv. Finl.* **15,** 43–59 (1992).
5. Legates, D. R. & Willmott, C. J. Mean seasonal and spatial variability in global surface air temperature. *Theor. Appl. Climatol.* **41,** 11–21 (1990).
6. Legates, D. R. & Willmott, C. J. Mean seasonal and spatial variability in gauge-corrected, global precipitation. *Int. J. Climatol.* **10,** 111–127 (1990).
7. Genthon, C. & Krinner, G. Antarctic surface mass balance and systematic biases in general circulation models. *J. Geophys. Res.* **106,** 20653–20664 (2001).
8. Krinner, G. & Werner, M. Impact of precipitation seasonality changes on isotopic signals in polar ice cores: A multi-model analysis. *Earth Planet. Sci. Lett.* **216,** 525–538 (2003).
9. Nelson, F. & Outcalt, S. I. A computational method for prediction and regionalization of permafrost. *Arct. Alp. Res.* **19,** 279–288 (1987).
10. Mangerud, J., Astakhov, V., Murray, A. & Svendsen, J. I. The chronology of a large ice-dammed lake and the Barents–Kara ice sheet advances, Northern Russia. *Glob. Planet. Change* **31,** 321–336 (2001).
11. Mangerud, J. *et al.* Ice-dammed lakes and rerouting of the drainage of northern Eurasia during the last glaciation. *Quat. Sci. Rev.* (in the press).
12. Thompson, S. L. & Pollard, D. Greenland and Antarctic mass balances for present and doubled atmospheric CO_2 from the GENESIS version-2 global climate model. *J. Clim.* **10,** 871–900 (1997).
13. Teller, J. T. in *The Quaternary Period in the United States* (eds Gillespie, A., Porter, S. & Atwater, B.) Ch. 3 (Elsevier, Amsterdam, 2003).
14. Khodri, M. *et al.* Simulating the amplification of orbital forcing by ocean feedbacks in the last glaciation. *Nature* **410,** 570–574 (2001).
15. de Noblet, N. *et al.* Possible role of atmosphere-biosphere interactions in triggering the last glaciation. *Geophys. Res. Lett.* **23,** 3191–3194 (1996).
16. Gallimore, R. G. & Kutzbach, J. E. Role of orbitally induced changes in tundra area in the onset of glaciation. *Nature* **381,** 503–505 (1996).
17. Shackleton, N. J. The 100,000-year ice-age cycle identified and found to lag temperature, carbon dioxide, and orbital eccentricity. *Science* **289,** 1897–1902 (2000).
18. Berger, A. Long-term variations of daily insolation and Quaternary climatic changes. *J. Atmos. Sci.* **35,** 2362–2367 (1978).
19. Clarke, G., Leverington, D., Teller, J. & Dyke, A. Superlakes, megafloods, and abrupt climate change. *Science* **301,** 922–923 (2003).
20. Krinner, G., Genthon, C., Li, L. & Le Van, P. Studies of the Antarctic climate using a stretched-grid general circulation model. *J. Geophys. Res.* **102,** 13731–13745 (1997).
21. Krinner, G. Impact of lakes and wetlands on boreal climate. *J. Geophys. Res. D* **108,** 101029/2002JD002597 (2003).
22. Petit, J.-R. *et al.* Climate and atmospheric history of the past 420,000 years from the Vostok ice core, Antarctica. *Nature* **399,** 426–436 (1999).
23. Siegert, M. J., Dowdeswell, J. A., Hald, M. & Svendsen, J. I. Modelling the Eurasian ice sheet through a full (Weichselian) glacial cycle. *Glob. Planet. Change* **31,** 367–385 (2001).
24. Marshall, S. J., Tarasov, L., Clarke, G. & Peltier, W. R. Glaciological reconstruction of the Laurentide Ice Sheet: Physical processes and modelling challenges. *Can. J. Earth Sci.* **37,** 769–793 (2000).
25. Charbit, S., Ritz, C. & Ramstein, G. Simulations of Northern Hemisphere ice-sheet retreat: Sensitivity to physical mechanisms involved during the Last Deglaciation. *Quat. Sci. Rev.* **21,** 243–266 (2002).
26. Crucifix, M., Loutre, M. F., Tulkens, P., Fichefet, T. & Berger, A. Climate evolution during the Holocene: a study with an Earth system model of intermediate complexity. *Clim. Dyn.* **19,** 43–60 (2002).
27. Crowley, T. Ice age terrestrial carbon changes revisited. *Glob. Biogeochem. Cycles* **9,** 377–389 (1995).

Acknowledgements We thank S. Hostetler for discussions and M. Siegert for comments and suggestions. Model simulations were carried out at IDRIS/CNRS. This work was supported by the ESF and the French national programmes ECLIPSE, PNEDC and ACI Jeunes Chercheurs. The field work and other analyses were funded by the Research Council of Norway by grants to the PECHORA project. M.J. was supported by NOAA.

Competing interests statement The authors declare that they have no competing financial interests.

Correspondence and requests for materials should be addressed to G.K. (krinner@ujf-grenoble.fr).

Natural examples of olivine lattice preferred orientation patterns with a flow-normal *a*-axis maximum

Tomoyuki Mizukami[1,2], Simon R. Wallis[2] & Junji Yamamoto[3]*

[1]*Department of Geology and Mineralogy, University of Kyoto, Sakyo-ku, Kyoto, 606-8501, Japan*
[2]*Department of Earth and Planetary Sciences, Graduate School of Environmental Studies, University of Nagoya, Chikusa-ku, Nagoya, 464-8601, Japan*
[3]*Laboratory of Earthquake Chemistry, University of Tokyo, Bunkyo-ku, Tokyo, 113-0033, Japan*

* Present address: Department of Earth and Planetary Sciences, Tokyo Institute of Technology, Meguro-ku, Tokyo, 152-8551, Japan

Tectonic plate motion is thought to cause solid-state plastic flow within the underlying upper mantle and accordingly lead to the development of a lattice preferred orientation of the constituent olivine crystals[1–3]. The mechanical anisotropy that results from such preferred orientation typically produces a direction of maximum seismic wave velocity parallel to the plate motion direction[4,5]. This has been explained by the existence of an olivine preferred orientation with an '*a*-axis' maximum parallel to the induced mantle flow direction[3,5,6–8]. In subduction zones, however, the olivine *a* axes have been inferred to be arranged roughly perpendicular to plate motion[9–13], which has usually been ascribed to localized complex mantle flow patterns[10–13]. Recent experimental work[14] suggests an alternative explanation: under conditions of high water activity, a 'B-type' olivine preferred orientation may form, with the *a*-axis maximum perpendicular to the flow direction. Natural examples of such B-type preferred orientation are, however, almost entirely unknown. Here we document widespread B-type olivine preferred orientation patterns from a subduction-type metamorphic belt in southwest Japan and show that these patterns developed in the presence of water. Our discovery implies that mantle flow above subduction zones may be much simpler than has generally been thought.

The Higashi-akaishi peridotite body of southwest Japan is the only kilometre-scale garnet peridotite body yet found in a subduction-type metamorphic belt[15]. This body offers an unrivalled opportunity to study subduction zone mantle directly. Here we focus on the olivine lattice preferred orientation (LPO) patterns of this body. The Higashi-akaishi body is tabular with an area of 10 km^2 and a thickness of 500 m (ref. 16) and occurs as an integral part of the Cretaceous Sanbagawa high-pressure, low-temperature metamorphic belt[17–19]. Dunite, a rock type of more than 90% olivine, is the main constituent of the body with minor amounts of wehrlite, pyroxenite, garnet pyroxenite, chromitite and garnet peridotite[15,16,20]. Serpentinized equivalents of these rock types developed in the periphery of the body[14] during exhumation, but the earlier olivine-rich microstructures and associated petrological information are well preserved in the inner part (Figs 1, 2).

Field observations and microstructural analyses allow two generations of tectonic fabrics to be distinguished in the dunite. The earliest D_1 fabric is defined by the crystal-shape preferred orientation of coarse clear olivine grains (~0.6 mm) (Fig. 1a). A second D_2 fabric is widespread throughout the Higashi-akaishi body and consists of coarse dusty olivine porphyroclasts (~0.5 mm) and fine clear olivine neoblasts (~0.1 mm) (Fig. 1c), which formed by dynamic recrystallization of the D_1 coarse-grained fabric (Fig. 1d). The preferred alignment of olivine crystals defines planar and linear fabrics for both D_1 (Fig. 1a) and D_2 (Fig. 1c). The olivine grain shape lineations are interpreted to be parallel to the maximum extension direction. This interpretation is supported by the common presence of elongate and boudinaged spinel grains with the same orientation. In many cases, field measurements of both planar and linear fabrics were cross-checked by multiple sectioning and microscopic observations of oriented samples. No significant difference was observed between the orientations determined in the field and those determined in the laboratory. The presence of composite planar and linear tectonic fabrics (L–S tectonites) implies roughly plane-strain conditions and, therefore, that the stretching lineation will approximate to the flow direction.

Both D_1 and D_2 are associated with well-developed and distinct olivine LPO patterns. Coarse-grained olivine of the D_1 fabric exhibits a girdle-type LPO with the *b*-axis concentration normal to the D_1 foliation and with a weak concentration of the *a* axis subparallel to the D_1 mineral lineation. In contrast, the olivine LPO associated with D_2 shows strong concentrations of the three crystallographic axes: with the *c*[001] axis subparallel to the stretching lineation, the *b*[010] axis subperpendicular to the tectonic foliation and the *a*[100] axis within the foliation and subperpendicular to the stretching lineation (Fig. 2b). This configuration is identical to the B-type LPO of ref. 14. The B-type LPO patterns and characteristic D_2 porphyroclastic microstructure are widely developed throughout the Higashi-akaishi body (Fig. 2a). In total, 12 such B-type fabrics were identified from 11 localities. The strongest B-type LPO patterns are found in the samples with the lowest proportion of D_1 porphyroclastic olivine, which we interpret to be the most deformed. Although there is some difference in strength, the topology of D_2 olivine LPO patterns is similar in both strongly and weakly deformed samples. We conclude that the LPO patterns, particularly those in the strongly deformed samples, closely approximate to steady-state fabrics and that the effects of earlier D_1 structures are negligible.

Porphyroclastic microstructures are commonly observed in deformed mantle xenoliths and peridotite bodies from various tectonic settings[21,22]. However, the D_2 porphyroclastic microstructure of the Higashi-akaishi body has several distinct features suggesting that it developed in the presence of water. The olivine porphyroclasts have a dusty appearance owing to micro-inclusions, whereas the neoblasts are clear (Fig. 1d). Similar microstructures have also been described in a previous study[23]. There are only very few inclusions in the pre-existing D_1 olivine (Fig. 1c), implying that the formation of micro-inclusions is related to the main D_2 deformation. High-powered microscopic study of 100-μm-thick sections revealed that most of these inclusions are two-phase inclusions with semi-faceted shapes and are commonly associated with radially arranged cracks in the host olivine crystal (Fig. 3a). Most cracks terminate within the host crystal and do not intersect grain boundaries. Micro-Raman spectroscopic analysis of the micro-inclusions detects a sharp band corresponding to the O–H stretching vibration at 3,650 cm^{-1} in Raman shift (Fig. 3b) with other peaks equivalent to those of serpentine. The sharp high frequency of the O–H stretching is consistent with a very weak hydrogen bond such as the hydroxyl ion of serpentine and not molecular H_2O. These observations suggest that the inclusions are the remains of water-rich fluid inclusions. The formation of the

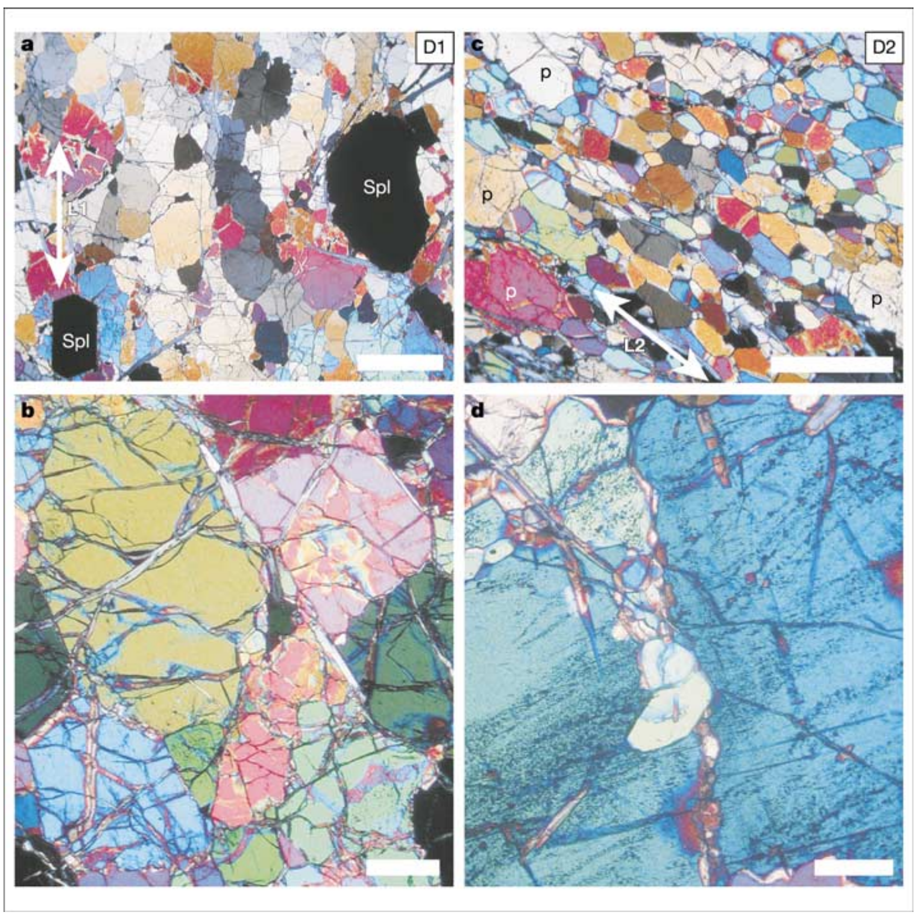

Figure 1 Photomicrographs of dunite in the Higashi-akaishi body (crossed polars). **a**, Coarse-grained D_1 dunite consisting of millimetre-sized olivine and Cr-spinel (Spl). A parallel alignment of their long axes defines a mineral lineation (L_1). Scale bar, 1.0 mm. **b**, Almost entirely inclusion-free D_1 olivine grains. Scale bar, 0.3 mm. **c**, Porphyroclastic dunite consisting of coarse porphyroclasts (p) and D_2 neoblasts of olivine. The grain shape of the D_2 olivine defines an L_2 lineation. Scale bar, 1.0 mm. **d**, D_2 neoblasts formed along subgrain boundaries within porphyroclasts. The olivine porphyroclasts contain abundant micro-inclusions. Scale bar, 0.1 mm.

cracks can be explained as the result of volumetric changes when the water reacted with the host olivine crystal to form serpentine. The ubiquitous occurrence of these inclusions in the D_2 porphyroclasts and their absence in D_1 olivine imply, therefore, that D_2 took place in the presence of water, a necessary condition for B-type LPO to develop. The water was probably supplied by dehydration reactions, which characterize much of the metamorphic changes in subducted crustal rocks.

The depth at which the B-type LPO patterns were formed can be constrained using a combination of petrological and microstructural methods. The solubility of alumina in orthopyroxene coexisting with garnet is one of the best-established and widely applied methods of estimating the formation pressure of mantle rocks[24]. Application of this geobarometer to the Higashi-akaishi body, combined with garnet-clinopyroxene and two-pyroxene geothermometers, has revealed a pressure–temperature evolution with a roughly isothermal burial at temperatures of 700–800 °C from a depth of 50 km to over 100 km (ref. 14). To relate this pressure–temperature history to the deformation stages and LPO patterns described above, we analysed the chemical compositions of orthopyroxene in a garnet peridotite in which both orthopyroxene and olivine have been dynamically recrystallized during the D_2 stage to form porphyroclasts and neoblasts. The Al content of orthopyroxene is lower in domains affected by D_2 deformation, such as the neoblasts, rims of porphyroclasts and boudinaged porphyroclasts, than in the cores of the porphyroclasts (Fig. 4). The decrease in the Al content of orthopyroxene during D_2 represents an increase in pressure and corresponds to the burial part of the pressure–temperature path derived for the Higashi-akaishi body. We conclude, therefore, that the D_2 deformation and associated olivine LPO formed under increasing pressure at depths between 50 and 100 km.

Thus we have found regionally developed B-type olivine LPO patterns characterized by an *a*-axis maximum perpendicular to the stretching direction. Microtextural and petrological data show that these LPO patterns developed at mantle depths greater than 50 km. The location of the Higashi-akaishi peridotite body at the highest structural levels of a subduction-type metamorphic belt, the pressure–temperature path and peak metamorphic conditions all strongly suggest that this unit represents a sliver of wedge mantle originally located above a subducting slab. This implies that D_2 and

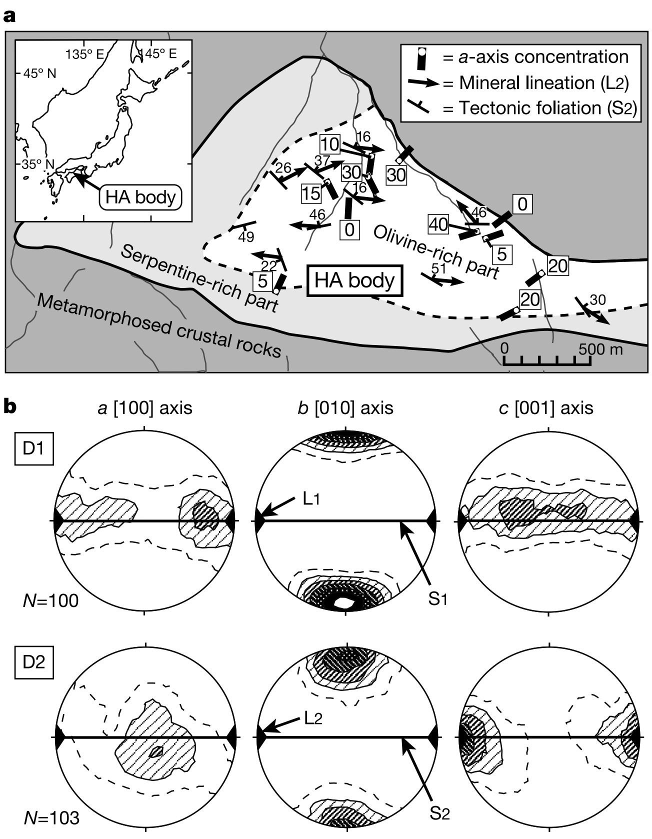

Figure 2 Structural analysis of olivine fabrics. **a**, Geological map of the Higashi-akaishi (HA) body showing representative D_2 structural data and the orientations of *a*-axis concentrations of the D_2 olivine LPO patterns. In each case the *a*-axis concentration is subperpendicular to the adjacent mineral lineation. Boxed numbers refer to the dips of the S_2 foliation and plunges of the *a*-axis concentrations. The LPO data include some measurements from ref. 16. **b**, Olivine LPO patterns of D_1 grains in coarse-grained dunite and of D_2 neoblasts in porphyroclastic dunite. The crystallographic axes are plotted with respect to the stretching lineation (L) and the tectonic foliation (S). *N*, number of measurements. Equal-area lower-hemisphere projection, with contours at 1 to 7 multiples of random concentration.

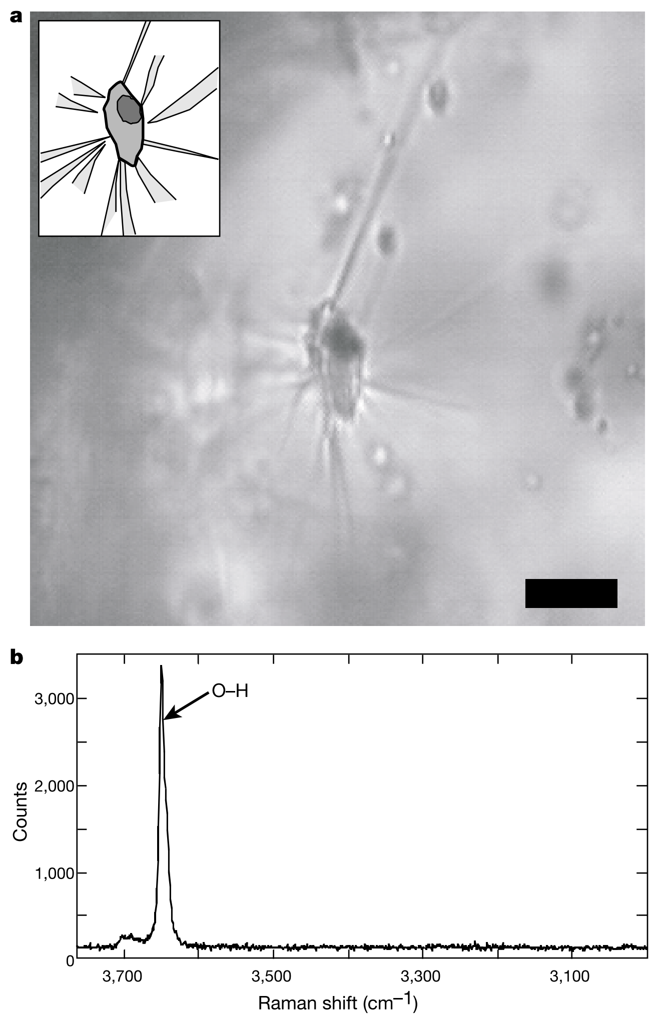

Figure 3 Micro-inclusions indicating the presence of water during the D_2 stage. **a**, Photomicrograph of micro-inclusions in olivine. An inclusion at the centre has a prismatic form, suggesting that it represents a negative crystal with the main fractures radiating from the apexes of the faceted surface. Raman spectroscopy shows that the light part of the inclusion and the surrounding fractures are filled by serpentine. Scale bar, 10 μm. **b**, Raman spectrum for the light part of the inclusion in **a**. A sharp peak at the wavenumber of 3,650 cm^{-1} shows the presence of O–H bonds as water of crystallization[25].

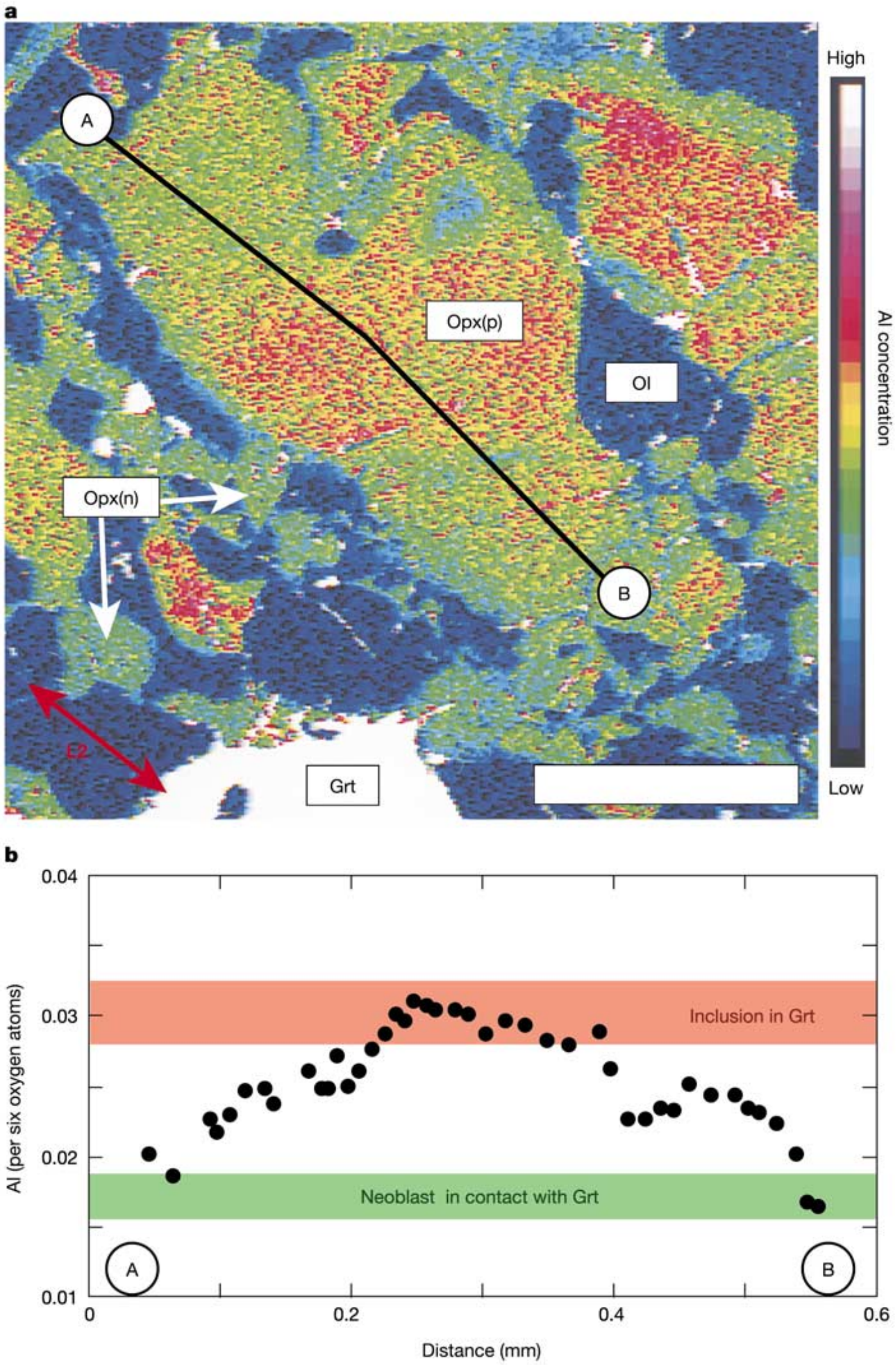

Figure 4 Mineral chemistry in garnet peridotite. **a**, X-ray elemental map using the Al Kα line for minerals in garnet peridotite. Colours in the bar at the right side correspond to the X-ray intensity. The areas of relatively low Al (greenish) tend to occupy the extensional sides of the porphyroclastic orthopyroxene (Opx-p). Al concentration is also low in the recrystallized neoblasts (Opx-n). In contrast, relatively high Al concentrations are found in the core. Ol, olivine; Grt, garnet. Scale bar, 0.2 mm. **b**, Line profile of Al content in the porphyroclastic orthopyroxene at the centre of **a**, determined using a microprobe.

the associated olivine LPO developed in subduction zone upper mantle.

Our results confirm the suggestion from experimental work[14] that B-type olivine LPO patterns can develop in the mantle wedge above subducting slabs in the presence of water. In most subduction zones the mantle wedge is likely to be infiltrated with water and to experience similar physical conditions to those recorded here. We suggest, therefore, that mantle deformation above subduction zones should, in general, be associated with B-type olivine LPOs. This general association can explain the anomalous seismic anisotropy in these regions and implies that mantle flow in these regions is parallel to plate motion, not perpendicular as has generally been thought[10–13]. This new constraint on mantle flow is essential to build realistic physical models of subduction zones. □

Received 7 June; accepted 3 November 2003; doi:10.1038/nature02179.

1. Nicolas, A. & Christensen, N. I. Formation of anisotropy in upper mantle peridotites—a review. In *Composition, Structure and Dynamics of the Lithosphere-Asthenosphere System* (eds Fuchs, K. & Froideoaux, C.) 111–123 (1987).
2. Carter, N. L. & Ave'Lallemant, H. G. High temperature flow of dunite and peridotite. *Geol. Soc. Am. Bull.* **81,** 2181–2202 (1970).
3. Zhang, S. & Karato, S. Lattice preferred orientation of olivine aggregates deformed in simple shear.

Nature **375,** 774–777 (1995).
4. Raitt, R. W., Shor, G. G., Francis, T. J. G. & Morris, G. B. Anisotropy of the Pacific upper mantle. *J. Geophys. Res.* **74,** 3095–3109 (1969).
5. Christensen, N. I. The magnitude, symmetry and origin of upper mantle anisotropy based on fabric analyses of ultramafic tectonites. *Geophys. J. R. Astron. Soc.* **76,** 89–111 (1984).
6. Hess, H. H. Seismic anisotropy of the uppermost mantle under oceans. *Nature* **203,** 629–631 (1964).
7. Francis, T. J. G. Generation of seismic anisotropy in the upper mantle along the mid-oceanic ridges. *Nature* **221,** 162–165 (1969).
8. Peselnick, L., Nicolas, A. & Stevenson, P. R. Velocity anisotropy in a mantle peridotite from the Ivrea zone: application to upper mantle anisotropy. *J. Geophys. Res.* **79,** 1175–1182 (1974).
9. Ando, M., Ishikawa, Y. & Yamazaki, F. Shear wave polarization anisotropy in the upper mantle beneath Honshu, Japan. *J. Geophys. Res.* **88,** 5850–5864 (1983).
10. Shih, X. R., Schneider, J. F. & Meyer, R. P. Polarities of P and S waves, and shear wave splitting observed from the Bucaramanga Nest, Colombia. *J. Geophys. Res.* **96,** 12069–12082 (1991).
11. Yang, X. & Fischer, K. M. Seismic anisotropy beneath the Shumagin Islands segment of the Aleutian-Alaska subduction zone. *J. Geophys. Res.* **100,** 18165–18177 (1995).
12. Fouth, M. J. & Fischer, K. M. Mantle anisotropy beneath northwest Pacific subduction zones. *J. Geophys. Res.* **101,** 15897–16002 (1996).
13. Smith, G. P. *et al.* A complex pattern of mantle flow in the Lau backarc. *Science* **292,** 713–716 (2001).
14. Jung, H. & Karato, S. Water-induced fabric transitions in olivine. *Science* **293,** 1460–1463 (2001).
15. Enami, M., Mizukami, T. & Yokoyama, K. Metamorphic evolution of garnet-bearing ultramafic rocks from the Gongen area, Sanbagawa belt, Japan. *J. Metamorph. Geol.* **22,** 1–15 (2004).
16. Yoshino, G. Structural-petrological studies of peridotite and associated rocks of the Higashi-akaishi-yama District, Shikoku, Japan. *J. Sci. Hiroshima Univ. C* **3,** 343–402 (1961).
17. Banno, S. & Sakai, C. Geology and metamorphic evolution of the Sanbagawa metamorphic belt, Japan. In *Evolution of Metamorphic Belts* (eds Daley, J. S., Cliff, R. A. & Yardley, B. W. D.) 519–532 (1989).
18. Takasu, A. & Dallmeyer, R. D. $^{40}Ar/^{39}Ar$ mineral age constraints for the tectonothermal evolution of the Sambagawa metamorphic belt, central Shikoku, Japan: a Cretaceous accretionary prism. *Tectonophysics* **185,** 111–139 (1990).
19. Wallis, S. Exhuming the Sanbagawa metamorphic belt: the importance of tectonic discontinuities. *J. Metamorph. Geol.* **16,** 83–95 (1998).
20. Mori, T. & Banno, S. Petrology of peridotite and garnet clinopyroxenite of the Mt. Higashi Akaishi mass, central Shikoku, Japan—subsolidus relation of anhydrous phases. *Contrib. Mineral. Petrol.* **41,** 301–323 (1973).
21. Mercier, J.-C. C. & Nicolas, A. Textures and fabrics of upper-mantle peridotites as illustrated by xenoliths from basalts. *J. Petrol.* **16,** 454–487 (1975).
22. Boudier, F. & Nicolas, A. Nature of the Moho transition zone in the Oman ophiolite. *J. Petrol.* **36,** 777–796 (1995).
23. Hirai, H. & Arai, S. H_2O–CO_2 fluids supplied in alpine-type mantle peridotites: electron petrology of relic fluid inclusions in olivines. *Earth Planet. Sci. Lett.* **85,** 311–318 (1987).
24. Harley, S. L. & Green, D. H. Garnet-orthopyroxene barometry for granulites and peridotites. *Nature* **300,** 697–701 (1982).
25. Rossman, G. R. Vibrational spectroscopy of hydrous components. *Rev. Mineral.* **18,** 193–206 (1988).

Acknowledgements S. Wallis aided in the field studies for this work and was closely involved in developing the rationale for the study. J. Yamamoto carried out the laser micro-Raman spectroscopic analyses. We thank H. Kagi for his support during these analyses and for discussion on this work. We also thank M. Enami and M. Obata for their comments. This work was supported in part by a grant from the Fukada Geological Institute.

Competing interests statement The authors declare that they have no competing financial interests.

Correspondence and requests for materials should be addressed to T.M. (mizukami@kueps.kyoto-u.ac.jp).

Friction falls towards zero in quartz rock as slip velocity approaches seismic rates

Giulio Di Toro[1], **David L. Goldsby**[2] **& Terry E. Tullis**[2]

[1]*Dipartimento di Geologia, Paleontologia e Geofisica, Universita' di Padova, Padova, 35137, Italy*
[2]*Department of Geological Sciences, Brown University, Providence, Rhode Island 02912, USA*

An important unsolved problem in earthquake mechanics is to determine the resistance to slip on faults in the Earth's crust during earthquakes[1]. Knowledge of coseismic slip resistance is critical for understanding the magnitude of shear-stress reduction and hence the near-fault acceleration that can occur during earthquakes, which affects the amount of damage that earthquakes are capable of causing. In particular, a long-unresolved problem is the apparently low strength of major faults[2–6], which may be caused by low coseismic frictional resistance[3]. The frictional properties of rocks at slip velocities up to 3 mm s^{-1} and for slip displacements characteristic of large earthquakes have been recently simulated under laboratory conditions[7]. Here we report data on quartz rocks that indicate an extraordinary progressive decrease in frictional resistance with increasing slip velocity above 1 mm s^{-1}. This reduction extrapolates to zero friction at seismic slip rates of ~1 m s^{-1}, and appears to be due to the formation of a thin layer of silica gel on the fault surface: it may explain the low strength of major faults during earthquakes.

There are significant experimental difficulties in determining the resistance to slip on faults during earthquakes. Laboratory experiments need to combine the high slip velocities V (0.1–2 m s^{-1}), large slip displacements δ (0–10 m) and high normal stresses σ_n (>50 MPa) that might be necessary to activate dynamic fault weakening mechanisms operative during earthquakes. All existing laboratory friction data satisfy at most two of these three criteria[7–13]. Values of the coefficient of friction μ for most rocks are relatively high over a wide range of normal stress; values of μ of ~0.6–0.85 are found when the slip velocity and displacement are ≤1 mm s^{-1} and <1 mm, respectively[9]. This high friction at ambient normal stresses in the Earth's continental crust is consistent with the magnitudes of shear stresses measured in the crust[14]. However, several mechanisms have been proposed that could lower shear resistance during fast coseismic slip, such as shear melting[11,12,15,16], pore fluid pressurization[3], normal interface vibrations[17], acoustic fluidization[18] and elastohydrodynamic lubrication[19]. Given all of these potential dynamic weakening mechanisms, it seems quite plausible that resistance during earthquake slip might be lower than implied by the high values of friction[9] measured at slow slip velocities. Nevertheless, these mechanisms and/or their applicability to earthquakes are still poorly understood; thus resistance to slip during earthquakes is still unknown.

To increase our understanding of coseismic slip resistance, we conducted rapid-slip experiments at ambient temperature and humidity in a servo-controlled compression–torsion apparatus. Sliding occurred during rotary shear of an annular surface oriented normal to the rotation axis. Experiments were performed on six samples of Arkansas novaculite (a quartz rock of meta-sedimentary origin[20] with a grain size of 1–5 μm) and one sample of granite. The upper, ring-shaped part of the sample, with a thickness of 2.56 mm and inner and outer radii of 22.2 and 26.97 mm, respectively, was slid on a lower circular plate of ~35 mm radius and ~8 mm thickness. Sliding surfaces were pre-roughened with no. 150 SiC grit to create a r.m.s. surface roughness of ~30 μm. Experiments were conducted at $\sigma_n = 5$ MPa. Temperatures were measured with a thermocouple embedded a distance of ~1 mm from the sliding surface in the upper sample ring. The rotary shear apparatus allows unidirectional sliding displacements of only ~40 mm; large cumulative displacements of up to 4,700 mm were achieved by repeatedly reversing the sliding direction (Fig. 1c). A constant slip velocity V in the range 1 μm s^{-1} to 100 mm s^{-1} was maintained during each experiment (Fig. 1b–d).

The experiments involved three steps: an initial 'loading' step to verify the low-speed behaviour, a 'high-speed' step to determine the velocity dependence, and a final 'recovery' step to determine whether and how the strength returned to typical low-speed values (Fig. 1a). During the loading step, the sample was slid at 1 μm s^{-1} for 1.2–2.0 mm of displacement. During this step, μ gradually increased from 0 to 0.7–0.8, then oscillated owing to 'stick-slip' sliding, as expected for the stiffness of the machine and the low-speed frictional behaviour of the rock[8]. In the high-speed step, V was abruptly increased and the sample was slid to large displacements, frequently up to ~4.5 m (Fig. 1a), during which friction decreased